communications physics

A Nature Portfolio journal

Article

https://doi.org/10.1038/s42005-025-02235-6

Pressure induced transition from chiral charge order to time-reversal symmetry-breaking superconducting state in Nb-doped CsV_3Sb_5

Jennifer N. Graham[1,11], Shams Sohel Islam[1,11], Vahid Sazgari[1], Yongka Li[2,3], Hanbin Deng[4], Gianluca Janka[1], Yigui Zhong[5], Orion Gerguri[1], Petr Král[1], Andrin Doll[1], Izabela Biało[6,7], Johan Chang[6], Zaher Salman[1], Andreas Suter[1], Thomas Prokscha[1], Yugui Yao[2,3,8], Kozo Okazaki[5,9,10], Hubertus Luetkens[1], Rustem Khasanov[1], Zhiwei Wang[2,3,8] ✉, Jia-Xin Yin[4] & Zurab Guguchia[1] ✉

Understanding how time-reversal symmetry (TRS) breaks in quantum materials is key to uncovering new states of matter and advancing quantum technologies. However, unraveling the interplay between TRS breaking, charge order, and superconductivity in kagome metals continues to be a compelling challenge. Here, we investigate the kagome metal $Cs(V_{1-x}Nb_x)_3Sb_5$ with $x = 0.07$ using muon spin rotation (μSR), alternating current (AC) magnetic susceptibility, and scanning tunneling microscopy (STM), under combined tuning by chemical doping, hydrostatic pressure, magnetic field, and depth from the surface. We find that TRS breaking in the bulk emerges below 40 K—lower than the charge order onset at 58 K—while near the surface, TRS breaking onsets at 58 K and is twice as strong. Niobium doping raises the superconducting critical temperature from 2.5 K to 4.4 K. Under pressure, both the critical temperature and superfluid density double, with TRS-breaking superconductivity appearing above 0.85 GPa. These findings reveal a depth-tunable TRS-breaking state and unconventional superconducting behavior in kagome systems.

Exchange interactions in quantum materials are often balanced in such a way that there is significant overlap between the superconducting, magnetic and topological phases[1–3]. However, if quantum materials are ever to mature into new technologies, an important question to ask is whether we can stabilise one phase by tuning the exchange interactions through internal or external parameters. The kagome lattice—a network of corner-sharing triangles—has been identified as a model system to explore such a question primarily due to its band structure, which uniquely combines flat bands, van Hove singularities and topological Dirac points, leading to a diverse set of quantum phases[2,4–8]. In this vein, the AV_3Sb_5 (A = K, Rb, Cs) compounds have been extensively studied and show several intriguing physical phenomena, including giant anomalous Hall effect, pair density waves and high-temperature time-reversal symmetry (TRS) breaking charge order[9–11]. The physics of the AV_3Sb_5 compounds is largely dictated by the competition or cooperation between two states, superconductivity and charge order. Extensive characterisation has shown that by suppressing the formation of charge order, the superfluid density and critical temperature, T_C can be increased, or vice versa. Depending on the system, previously tuning parameters have included external magnetic fields, hydrostatic pressure and depth-dependent studies[5,10,12,13].

[1]PSI Center for Neutron and Muon Sciences CNM, Villigen PSI, Switzerland. [2]Key Laboratory of Advanced Optoelectronic Quantum Architecture and Measurement, Ministry of Education, School of Physics, Beijing Institute of Technology, Beijing, China. [3]Beijing Key Lab of Nanophotonics and Ultrafine Optoelectronic Systems, Beijing Institute of Technology, Beijing, China. [4]Department of Physics, Southern University of Science and Technology, Shenzhen, Guangdong, China. [5]Institute for Solid States Physics, The University of Tokyo, Kashiwa, Japan. [6]Physik-Institut, Universität Zürich, Zürich, Switzerland. [7]AGH University of Science and Technology, Faculty of Physics and Applied Computer Science, Kraków, Poland. [8]International Center for Quantum Materials, Beijing Institute of Technology, Zhuhai, China. [9]Trans-scale Quantum Science Institute, The University of Tokyo, Tokyo, Japan. [10]Material Innovation Research Center, The University of Tokyo, Kashiwa, Japan. [11]These authors contributed equally: Jennifer N. Graham, Shams Sohel Islam. ✉e-mail: zhiweiwang@bit.edu.cn; zurab.guguchia@psi.ch

Another tuning parameter is chemical doping, and lately it has been shown that these two key phases can be controlled by doping with small amounts of several elements, including Ta, As, Mo, Ti and Nb[14–20]. In each case, the dopant resides solely in the V-kagome layer, which suggests doping will always produce some effect on the magnetism[21–23], however this effect is highly dependent on the dopant itself. For example, undoped CsV_3Sb_5 develops charge order at $T_{CO} \approx 90$ K, and a superconducting transition at $T_C = 2.5$ K[24]. Doping with 14% Ta[19] or 4.7% Ti[17] was successful in fully suppressing the formation of the charge order, after which the T_C of the Ta compound was increased to 5.2 K. This is akin to applying hydrostatic pressure to undoped CsV_3Sb_5[11,12,25]. Meanwhile, doping with 7% Nb[19] partially suppresses the formation of charge order from 90 to 58 K, but raises T_C from 2.5 to 4.4 K.

Inspired by these results, we have chosen to focus on one particular stoichiometry, $Cs(V_{0.93}Nb_{0.07})_3Sb_5$ ($Nb_{0.07}$-CVS), which is the current limit of Nb doping into CsV_3Sb_5[19]. Recent angle-resolved photoelectron spectroscopy (ARPES) results revealed $Nb_{0.07}$-CVS has a nodeless, nearly isotropic and orbital-independent superconducting gap[19]; however, there lacks a detailed microscopic investigation into the superfluid density and how we can manipulate the microscopic properties of both the superconducting and normal states of $Nb_{0.07}$-CVS, which we aim to address in this article. In the following, we employ a unique combination of muon spin rotation/relaxation (μSR) techniques to investigate the temperature, field and depth dependence of the magnetic penetration depth and possible TRS breaking effects in the normal state. We also introduce another powerful tuning parameter, hydrostatic pressure, which we find has a strong influence on the superconducting properties of $Nb_{0.07}$-CVS, and we have constructed the phase diagram up to 2 GPa of applied pressure. Although the effect of these tuning parameters has been explored in other kagome systems, to the best of our knowledge, this is the first time all have been combined into a single study. This unique approach has revealed key features of the kagome system $Nb_{0.07}$-CVS. Our results show that Nb-doping decouples TRS breaking from charge order in the bulk, whilst aligning them near the surface. Under the application of low hydrostatic pressure (but still sufficient to suppress the charge order), the system transitions to a superconducting state with two notable unconventional features: (1) time-reversal symmetry breaking below T_c accompanied by nodeless electron pairing, pointing to chiral superconductivity and (2) an unusual correlation between the superconducting critical temperature and the superfluid density.

Results

Unconventional normal state

Polycrystalline and single-crystal samples of $Nb_{0.07}$-CVS were synthesised according to other reports[19]. Unless otherwise stated, measurements were performed on single-crystal samples. Firstly, Fig. 1 shows a summary of scanning tunnelling microscopy (STM) measurements that were collected at a lattice temperature of 30 mK. Figure 1a shows individual Nb dopants that are atomically resolved and consistent with the target dopant level of 7%. A lower bias voltage of 20 meV, reveals that $Nb_{0.07}$-CVS is subject to a 2×2 chiral charge order, as indicated by the vector peaks (red circles) in the inset of Fig. 1b. This is the same charge order as the parent undoped compound, CsV_3Sb_5, however, the gap is reduced to 20 meV (Fig. 1c), as compared to 40 meV for CsV_3Sb_5[26]. Furthermore, the STM results reveal an isotropic superconducting gap of 0.64 meV (Fig. 1d). The fully opened superconducting gap in Nb- or Ta-doped CVS is also consistent with our ARPES and μSR results[19]. This behavior contrasts with the parent compounds, where STM measurements[8,27,28] detect a residual density of states, interpreted as Bogoliubov–Fermi surfaces associated with pair-density wave (PDW) order.

One of the benefits of μSR is the ability to detect internal magnetic fields as small as 0.01 mT, without the need for the application of an external field, and it is therefore an ideal tool to study the spontaneous fields that may arise due to TRS breaking in unconventional superconductors. Therefore, zero-field (ZF)-μSR measurements were conducted over a wide temperature range. A summary of the ZF-μSR measurements performed in the normal

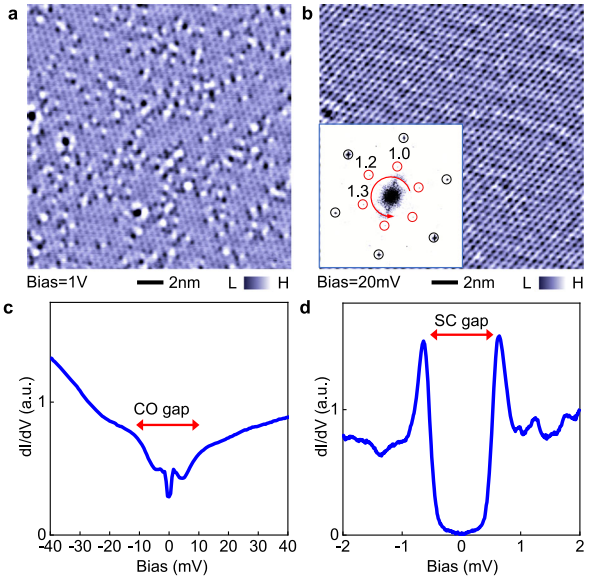

Fig. 1 | Scanning tunnelling microscopy measurements of $Cs(V_{0.93}Nb_{0.07})_3Sb_5$. **a** Topographic image with high bias voltage showing the individual Nb dopants (dark spots). **b** Topographic image with low bias voltage at the same atomic location. The inset shows its Fourier transform, demonstrating the 2×2 charge order vector peaks (red circles). **c** Differential tunnelling spectrum showing a gap of 20 meV caused by the charge order. The spectrum is measured over a wide energy scale with a low energy resolution; the excitation voltage of the lock-in is set to be large, so that it smears out the superconducting gap structure. **d** Differential tunnelling spectrum showing superconducting gap of 0.64 meV. The density of states does drop to zero at zero bias. All the data were collected at a lattice temperature of 30 mK.

state of $Nb_{0.07}$-CVS are shown in Fig. 2a and b and provides evidence of TRS breaking within the charge-ordered state. Figure 2a presents μSR measurements at 5 K in ZF and longitudinal fields (LF-field is applied parallel to the muon spin polarisation) up to 20 mT. To be consistent with previous works, the ZF data were fit with a Gaussian Kubo-Toyabe depolarisation function multiplied by an exponential term[29]:

$$A_{ZF}^{GKT}(t) = \left(\frac{1}{3} + \frac{2}{3}(1-\sigma^2 t^2)\exp\left[-\frac{\sigma^2 t^2}{2}\right]\right)\exp(-\Gamma t) + A_{bkg} \quad (1)$$

where σ/γ_μ ($\gamma_\mu/2\pi = 135.5$ MHz/T is the muon gyromagnetic ratio) is the width of the local field distribution primarily due to the nuclear moments, σ and Γ are muon spin relaxation rates, and A_{bkg} is a small, constant background term. The exponential relaxation rate Γ can be due to a mixture of dilute and dense nuclear moments, the presence of electric field gradients or a contribution of electronic origin. The full polarization can be recovered by the application of a small external longitudinal magnetic field of 20 mT. This highlights that the relaxation is due to spontaneous fields, which are static on the microsecond timescale.

Figure 2b shows the evolution of the σ and Γ rates across a wide temperature range measured in ZF conditions. Whilst the Gaussian σ component remains nearly temperature-independent, displaying only a subtle, non-monotonic behaviour below 60 K, a noticeable increase occurs below $T^* = 40$ K for the Γ rate. It is noteworthy that this single-step increase of Γ is different from the two-step transition which has been seen in μSR studies of undoped CsV_3Sb_5[30], undoped RbV_3Sb_5[10,31] and other kagome-based compounds[10,32]. The increase in the exponential relaxation below T^* is estimated to be $\simeq 0.025\ \mu s^{-1}$, which can be interpreted as a characteristic field strength $\Gamma_{12}/\gamma_\mu \simeq 0.05$ mT. However, in the present case, these ZF-μSR results alone do not provide conclusive evidence for time-reversal symmetry-breaking in $Nb_{0.07}$-CVS below T^*. The onset of charge order or charge redistribution might also alter the electric field gradient experienced

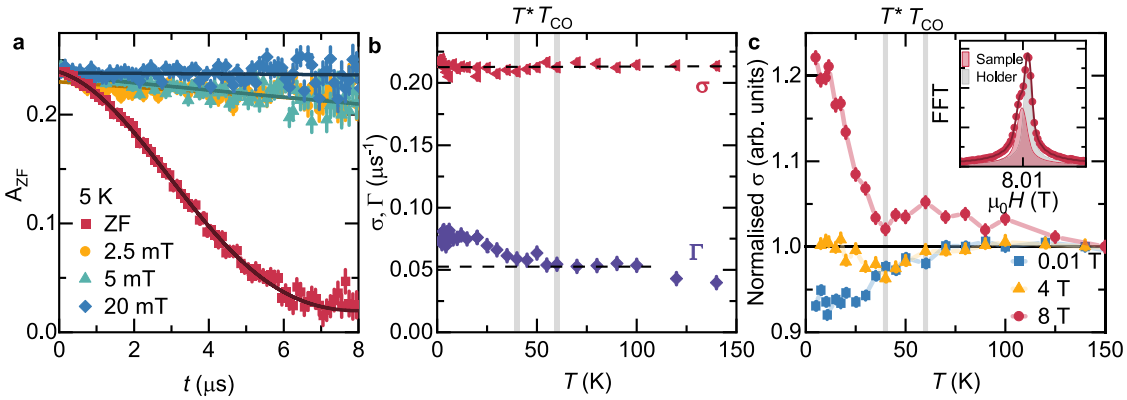

Fig. 2 | Summary of muon-spin rotation (μSR) experiments in the normal state of $Cs(V_{0.93}Nb_{0.07})_3Sb_5$ ($Nb_{0.07}$-CVS). a Zero-field (ZF) and longitudinal-field (LF) μSR spectra measured at 5 K in various fields up to 20 mT. The error bars are the standard error of the mean (s.e.m.) in about 10^6 events. **b** Evolution of σ (red triangles) and Γ (purple diamonds) relaxation rates as a function of temperature in the normal state. An increase in the Γ relaxation below T_{CO} implies time-reversal symmetry (TRS) breaking is present in $Nb_{0.07}$-CVS. The error bars represent the standard deviation of the fit parameters. **c** Evolution of σ relaxation rate under applied fields of 0.01 T (blue squares), 4 T (yellow triangles) and 8 T (red circles). Inset shows the Fourier transform of the 8 T data at 5 K, which has been fit with two components; the sample (red) and the silver holder (grey).

by the nuclei and, correspondingly, the magnetic dipolar coupling of the muon to the nuclei. This can induce a change in the nuclear dipolar contribution to the ZF μSR signal. In order to substantiate the above ZF μSR results, systematic high-field μSR[10,32] experiments are therefore essential. In a strong magnetic field, the applied field determines the quantization axis for the nuclear moments, rendering the influence of charge order on the electric field gradient at the nuclear sites negligible.

To confirm the magnetic origin of the increase in Γ, we performed transverse-field (TF)-μSR measurements under applied magnetic fields up to 8 T, as shown in Fig. 2c. In TF-μSR, it is difficult to distinguish between the σ and Γ components, so instead the relaxation is described by a single effective rate, σ. In a field of 0.01 T, a small non-monotonous dip in σ is observed, which is similar to the dominant σ_{ZF} rate in Fig. 2b. However, at higher TFs, such as 4 and 8 T, the rate shows a clear increase at lower temperatures in the charge-ordered state, which is reminiscent of the behaviour of Γ in zero-field. As the nuclear contribution to the relaxation rate cannot be enhanced by an external field, this indicates the increase at low temperatures is dominated by the electronic contribution. In particular, at 8 T, there is a sizeable enhancement of σ below $T^* = 40$K, which is relatively larger for $Nb_{0.07}$-CVS compared to undoped CsV_3Sb_5[30]. The non-linear scaling of σ with applied field has also been observed in other kagome compounds, such as KV_3Sb_5[33], but currently, there is no theoretical understanding of this phenomenon. The inset shows the Fourier transform of the 8 T data at 5 K, where a clear splitting and broadening of the peak is visible. The narrow signal arises from the silver sample holder. The broad signal (red), with the fast relaxation, is shifted towards lower fields from the applied one, arises from the muons stopping in the sample and takes a majority fraction (70–80%) of the μSR signal. This points to the fact that the sample response arises from the bulk of the sample. The combined results of ZF-μSR and high-field μSR reveal an enhanced internal field width below $T^* = 40$ K, providing direct evidence of time-reversal symmetry-breaking fields within the kagome lattice. Notably, the onset of TRS breaking occurs at a lower temperature than the expected ordering temperature, $T_{CO} = 58$ K. This indicates a splitting of these two temperatures in the bulk of the doped kagome system, a behaviour distinct from that observed in undoped compounds.

The measurements above are all presented from a bulk perspective. However, our recent studies have shown that TRS breaking is enhanced near the surface region of undoped RbV_3Sb_5 systems with optimal charge order[13]. We also demonstrated that in Ta-doped CsV_3Sb_5, where charge order is suppressed, no surface enhancement was observed. These findings, therefore, motivate a depth-dependent investigation of $Nb_{0.07}$-CVS, to explore whether the surface effect persists under the partial suppression of charge order. This is achieved through a combination of ZF and weak TF μSR measurements. Figure 3a shows the muon implantation profile for $Nb_{0.07}$-CVS for various implantation energies, simulated using the Monte Carlo algorithm TrimSP[34]. By varying the implantation depth of the muon we can therefore probe different depths of $Nb_{0.07}$-CVS. The ZF-μSR spectra are shown in Fig. 3b at both the surface ($E = 2$ keV, corresponding to a mean implantation depth, $\bar{z} = 10$ nm) and in the bulk ($E = 16$ keV, $\bar{z} = 100$ nm). A noticeable difference in the shape of the field distribution is clearly visible between these two depths. The ZF data were analysed using Eq. (1), but whereas the spectrum measured in the bulk had both σ and Γ contributions, near the surface, the Gaussian σ component vanishes, leaving only the exponential Γ with a significant value. This is also evident qualitatively from the time spectra, which display a clear exponential form. Additionally, near the surface, the muon can be decoupled by applying a small external magnetic field longitudinally aligned with the muon spin polarization ($B_{LF} = 10$ mT). This shows that stronger static magnetism exists nearer the surface. Figure 3c presents the temperature dependence of the relaxation rate, Γ in both ZF and TF measurements at the surface (green) and in the bulk (purple). To account for differences in background, this is shown in terms of the differences, $\Delta\Gamma = \Gamma(T) - \Gamma(150\ \mathrm{K})$. In contrast to the bulk, at the surface there is a clear shift in the onset of TRS breaking towards higher temperatures, around the previously determined charge ordering temperature, $T_{CO} = 58$ K. This indicates that charge order and TRS breaking are more in sync at the surface but decoupled in the bulk. Importantly, the signal near the surface nearly doubles and continues to increase down to the lowest measured temperatures. Similar results were also observed in RbV_3Sb_5[13]; however, the response near the surface was stronger by a factor of 1.5 in RbV_3Sb_5 as compared to $Nb_{0.07}$-CVS. This suggests that the strength of the TRS breaking signal correlates with the onset/strength of charge order in these kagome superconductors. Finally, we measured the relaxation rate as a function of energy, which is shown in Fig. 3d. These results highlight that the surface effects are confined to very near the surface with a characteristic depth of $\bar{z}_c \simeq 20$ nm, which is shorter than the study on RbV_3Sb_5 ($\bar{z}_c \simeq 33$ nm)[13]. This is significant, as it identifies a characteristic depth below which the material's properties differ from those of the bulk, which in the case of $Nb_{0.07}$-CVS is confined nearer to the surface.

Unconventional superconducting state

Next, we explored the microscopic superconducting properties of $Nb_{0.07}$-CVS at ambient and under hydrostatic pressures. A summary of the weak TF measurements in ambient conditions are shown in Fig. 4, which show that $Nb_{0.07}$-CVS has a bulk superconducting state, a dilute superfluid density and single nodeless superconducting gap structure.

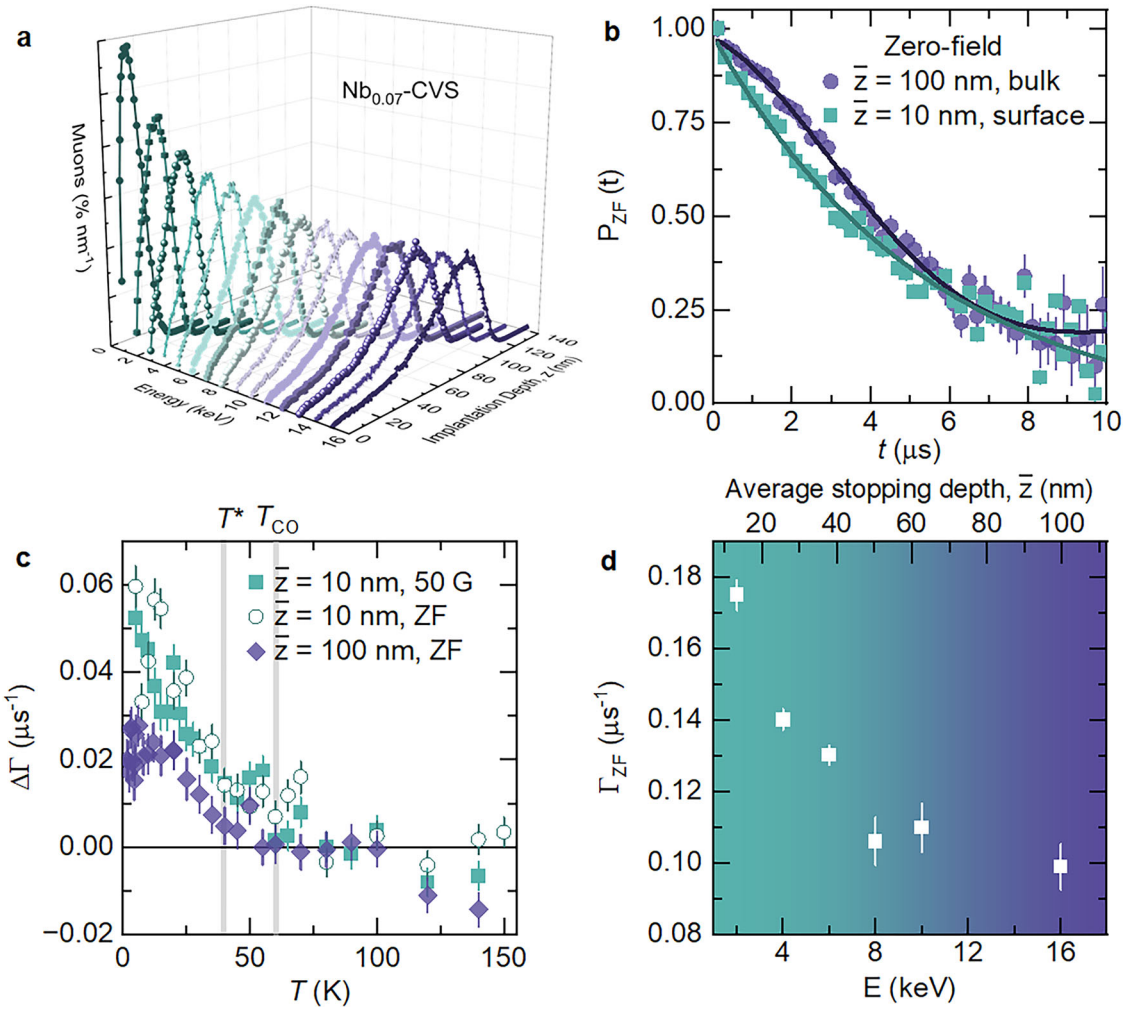

Fig. 3 | Depth-dependent magnetism in $Cs(V_{0.93}Nb_{0.07})_3Sb_5$ ($Nb_{0.07}$-CVS). **a** Muon implantation profile simulated for several energies. **b** Zero-field (ZF) muon-spin rotation (μSR) spectra for $Nb_{0.07}$-CVS. obtained at 5 K at the surface (mean implantation depth, $\bar{z} = 10$ nm, green) and in the bulk ($\bar{z} = 100$ nm, purple). The error bars are the standard error of the mean (s.e.m.) in about 10^6 events. **c** Temperature dependence of the relaxation rate, Γ measured in 50 G and zero-field at the surface ($\bar{z} = 10$ nm, green), and zero-field in the bulk ($\bar{z} = 100$ nm, purple). The high-temperature relaxation rate has been subtracted to put all data on a comparable scale. The error bars represent the standard deviation of the fit parameters. **d** The zero-field muon-spin relaxation rate measured at 5K in an applied field of 5 mT as a function of muon implantation energy, E. Top axis shows the mean implantation depth, $\bar{z}$. Green to purple shading depicts the transition from near-surface to bulk behaviour.

Firstly, in Fig. 4a, measurements above (purple, 10 K) and below (red, 1.5 K) T_C show the expected response from a superconductor; a weakly relaxing oscillation above T_C due to the random local fields produced by the nuclear moments, which is strongly enhanced below T_C due to the formation of the flux line lattice (FLL). This is further evident in Fig. 4b, which shows the Fourier transform of the μSR spectra, which is sharp and symmetric above T_C, but broadens and splits away from the applied field below T_C. These data were analysed using the following functional form[29]:

$$A_{TF}(t) = \sum_{i}^{n} A_{S,i} e^{\left[-\frac{(\sigma_{tot,i}t)^2}{2}\right]} \cos(\gamma_\mu B_{int,i} t + \phi_i) \quad (2)$$

where A_S is the initial asymmetry, σ_{tot} is the total muon spin depolarisation rate, $\gamma_\mu/(2\pi) \simeq 135.5$ MHz/T is the gyromagnetic ratio of the muon, B_{int} is the internal magnetic field, and ϕ is the initial phase shift of the muon ensemble. Data above T_C were fit with one component, whilst data below T_C were fit with three components; two originating entirely from the sample and making up 89.4%, with the third originating from the sample mount. Furthermore, below T_C, a clear decrease in the internal field is observed, consistent with the expected diamagnetic response of a superconductor. Taken together, these results not only confirm the bulk nature of superconductivity in $Nb_{0.07}$-CVS but also underscore the sample quality, as no anomalous increase in the internal field, indicating non-superconducting regions, is observed below T_C.

One of the most important measurable quantities in a μSR experiment on a superconductor is the muon spin depolarisation rate, $\sigma_{tot}(= \sqrt{\sigma_{sc}^2 + \sigma_{nm}^2})$, which is comprised of superconducting, σ_{sc} and nuclear magnetic dipolar, σ_{nm} contributions, as σ_{sc} is directly proportional to the superfluid density, and as a result, representative of the superconducting gap structure. The superconducting relaxation rate, σ_{sc} (Fig. 4c), was estimated by assuming the nuclear, σ_{nm}, contribution was constant above T_C and subtracting this value in quadrature from σ_{tot}. This measurement confirms $T_C \sim 4.5$ K, and shows that, like other kagome-based superconductors, $Nb_{0.07}$-CVS has a dilute superfluid density, with the ratio $T_C/\lambda_{ab}^{-2} \simeq 0.45$[5,12]—a hallmark feature of unconventional superconductivity. The topology of the superconducting gap structure is dependent on the temperature-dependent behaviour of the superfluid density, and since the data plateau below ~1 K implies that a nodeless gap structure will be the most appropriate. This was confirmed through fitting the data, where it was found that in ambient conditions $Nb_{0.07}$-CVS has a $T_C = 4.70(3)$ K, London penetration depth, $\lambda = 316(5)$ nm, and gap size,

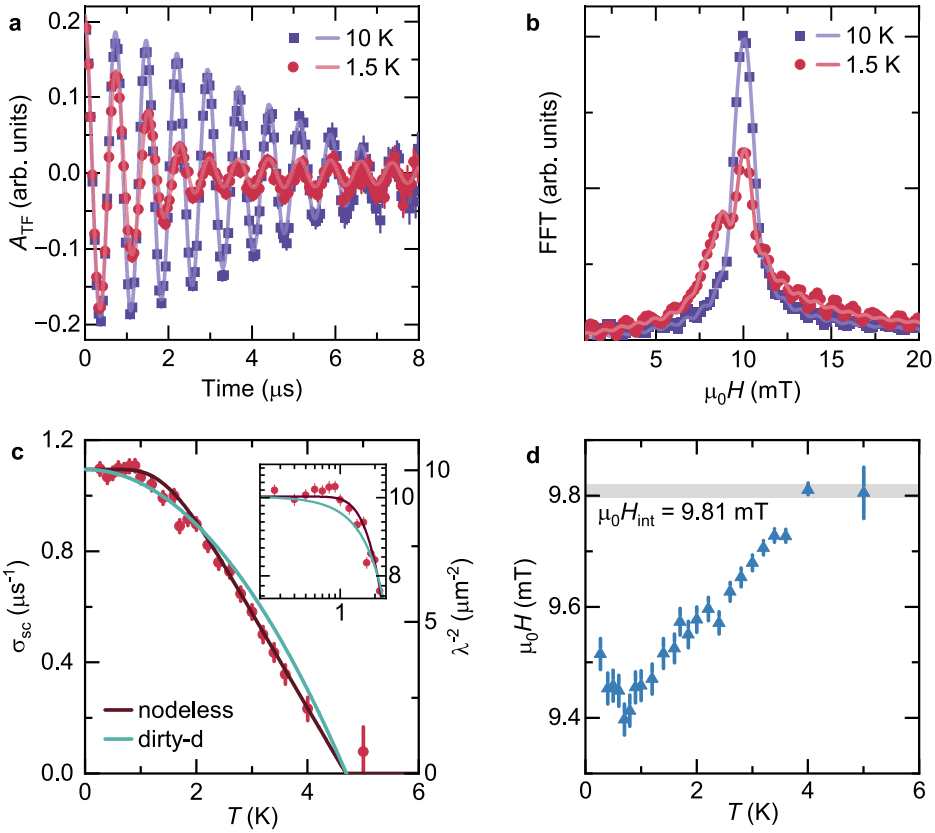

Fig. 4 | Summary of muon-spin rotation (μSR) experiments in the superconducting state of $Cs(V_{0.93}Nb_{0.07})_3Sb_5$. **a** Transverse-field (TF) μSR spectra collected above (10 K, purple) and below (1.5 K, red) T_C after field-cooling the sample from above T_C in an applied field of 10mT. The error bars are the standard error of the mean (s.e.m.) in about 10^6 events. **b** Fourier transforms of the data from (**a**). **c** Temperature dependence of the superconducting muon spin depolarisation rate, σ_{sc} and inverse squared penetration depth, λ^{-2} measured in 10 mT. The red and green solid lines show the fit of a nodeless *s*-wave gap and dirty-d wave model, respectively. The inset shows λ^{-2} against the low-temperature data on a log–log scale. The error bars represent the standard deviation of the fit parameters. **d** Response of the internal magnetic field, $\mu_0 H_{int}$, in the superconducting state has the expected diamagnetic shift.

$\Delta = 0.590(5)$ meV. Additionally, we have compared the nodeless model to a dirty *d*-wave, which is an alternative model that may describe the data. A superconductor with a dirty *d*-wave symmetry is one where there is significant disordered spin singlets and has a power law dependence as given by $A[1-(T/T_C)^2]$, where A is a scaling constant[35]. For our analysis, we fixed T_C to the experimentally determined value of 4.7 K, however, this model underfits the data, particularly at low temperatures where the data saturate. Therefore, the most accurate model for the superconducting gap structure of $Nb_{0.07}$-CVS is the nodeless gap structure, which is also in agreement with the STM results in Fig. 1d, which show an isotropic gap of 0.64 meV, and the previously performed ARPES measurements[19] (see also the Supplementary Note 2 and the Supplementary Fig. S2).

An additional tuning parameter is pressure, which for kagome superconductors has a varied response, from none in $LaRu_3Si_2$[32] to significantly enhancing the superconducting properties in the AV_3Sb_5 compounds[12,18,36]. Extending these investigations to include chemically doped samples is thus crucial to understanding the mechanisms that underpin these behaviours. Figure 5 displays an AC susceptibility and μSR study on the effect of hydrostatic pressure on $Nb_{0.07}$-CVS, which shows a strong response. In ambient and low applied pressures (<0.4 GPa), the AC susceptibility confirms T_C as ~4.5 K. Increasing the pressure to 1.2 GPa, leads to a large increase in the superfluid density and T_C to 7K. Between these two distinct phases, we have also measured at 0.8 GPa, which lies directly on the phase boundary. Intriguingly, the superfluid density has a broadened shape, incorporating elements from both the high and low T_C phases. The data at 0.8 GPa were therefore modelled with two nodeless gaps, as described in Table 1. It should be emphasised that this is not a change in the gap structure, but rather a more quantitative way to show that the data measured at 0.8 GPa is on the phase boundary. It is notable that the agreement between the AC susceptibility and μSR data is better for higher pressures (0.8 and 1.2 GPa) than the lower pressures (0 and 0.4 GPa) which is due to μSR being a bulk probe so the transition to the superconducting state is usually only visible once the majority of the sample is superconducting (eg. at the tail end of the susceptibility curve). For the 1.2 GPa data, it can be seen that the transition in the AC susceptibility is much sharper than the ambient pressure data, and therefore, T_C is more in agreement between μSR and AC susceptibility. Furthermore, the μSR data were collected under an applied field of 10 mT, whilst the AC data were collected under zero-field conditions, and this difference in experimental conditions can also result in some modification of T_C. Table 1 summarises the strong tuning ability of pressure in $Nb_{0.07}$-CVS, as between ambient and 1.2 GPa, the superfluid density has doubled, the gap size has tripled from ~0.5 to 1.5 meV, and there is a substantial increase in T_C from 4.5 to 7 K.

By systematically measuring more AC susceptibility data under pressure, we have been able to construct the pressure phase diagram of $Nb_{0.07}$-CVS as shown in Fig. 6a (full data in the Supplementary Note 1 and the Supplementary Fig. S1). This phase diagram shows the evolution of T_C from the measured AC susceptibility, normalised between −1 and 0 (as given by the colour bar) as a function of applied hydrostatic pressure. The transition from superconducting (blue) to normal (red) state can clearly be seen, with the broadness of the transition reflected in the width between the two. Here, we can clearly divide the behaviour of $Nb_{0.07}$-CVS into three regions: (I) the low-pressure region—$p < 0.5$ GPa where there is a sharp transition at T_C = 4.5K, (II) a mixed region—$0.5 < p < 0.85$ GPa where the transition becomes very broad and nondescript, and (III) the high pressure region—$p > 0.85$ GPa where there is a sharp transition at $T_C = 7$ K. These observations are quantitatively supported by the μSR measurements in Fig. 5b and Table 1, both in terms of T_C and the nature of the gap, which goes from single nodeless (I), to a double nodeless gap (II—reflecting the broadness of the transition), and back to a single nodeless gap (III). Also included in Fig. 6 are the inverse penetration depths, λ^{-2} (right axis, open circles) obtained from the gap structure analysis of the μSR data, which mirror the evolution of T_C very well and indicate nearly linear scaling between T_C and superfluid density.

Next, it is crucial to investigate whether the superconducting state breaks time-reversal symmetry. To address this, we employed ZF-μSR

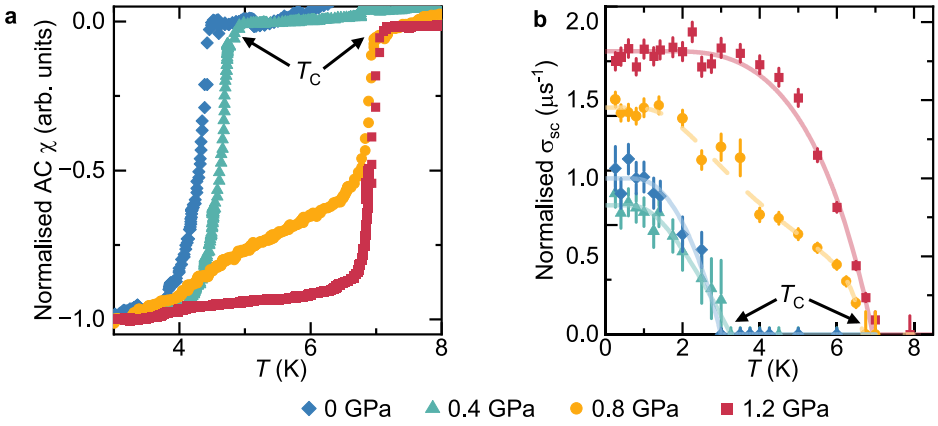

Fig. 5 | Tuning superconductivity in $Cs(V_{0.93}Nb_{0.07})_3Sb_5$ with pressure. a AC magnetic susceptibility, χ under various applied hydrostatic pressures. Data is normalised between −1 and 0. **b** Temperature dependence of normalised superconducting muon spin depolarisation rates, σ_{sc} measured in an applied field of $\mu_0 H = 10$ mT at ambient and various applied hydrostatic pressures. The superconducting gap symmetries have been determined as single nodeless *s*-wave (solid lines) with the exception of 0.8 GPa, which sits on the boundary between the two phases and was subsequently modelled with two *s*-wave gaps (dashed line). The error bars represent the standard deviation of the fit parameters.

analysis. Since charge order already breaks TRS at a temperature $T^* \sim T_{CO} \gg T_c$, suppressing the charge order transition temperature (T_{CO}) is essential, which may be achieved by applying pressure. Above 0.85 GPa, the pressure brings the system into the optimal T_c region of the phase diagram, where charge order is fully suppressed (see Fig. 6). In Fig. 6b, we present the internal field width Γ, derived from ZF-μSR data, across the superconducting transition for $Nb_{0.07}$-CVS measured at 1.2 and 1.5 GPa in single-crystal and polycrystalline samples, respectively. Notably, there is a significant enhancement in Γ, akin to that observed in superconductors that are believed to spontaneously break TRS, such as Sr_2RuO_4[37]. A similar increase in Γ below T_C is also observed for the undoped compound CsV_3Sb_5 at $p = 1.78$ GPa and for Ta-doped CsV_3Sb_5, both exhibiting fully suppressed charge order[12,13]. If there was a charge order remaining, then we would expect to see a sharp jump/drop in $\Delta\Gamma$ at T_c due to competition between superconductivity and internal fields from charge order. Crucially, in all compounds, we see a smooth increase in $\Delta\Gamma$, which is strong evidence to support TRS-breaking superconducting states in Cs-derived kagome superconductors and aligns with findings in KV_3Sb_5 and RbV_3Sb_5, indicating an unconventional pairing state.

If charge order were still present, we would expect the relaxation rate to increase above T_c, with a sharp anomaly at the transition due to competing internal fields from charge order and superconductivity.

Discussion

Our comprehensive investigation into the superconducting and normal-state properties of $Nb_{0.07}$-CVS has yielded three key findings:

(1) By combining zero-field and high-field muon spin rotation (μSR) measurements, we observed that time-reversal symmetry (TRS) breaking in the bulk of $Nb_{0.07}$-CVS (at depths >20 nm from the surface) occurs below $T^* = 40$ K, which is lower than the charge order onset temperature, $T_{CO} = 58$ K. In contrast, near the surface (within 20 nm), the TRS breaking signal is doubled in intensity and onsets at T_{CO}, suggesting that Nb doping decouples TRS breaking from charge order in the bulk, while these phenomena remain synchronized at the surface. This behaviour contrasts with observations in the undoped CsV_3Sb_5 system, where we detected a two-step increase in the muon spin relaxation rate at $T_{CO} = 90$ and 30 K[10,30]. In the undoped system, the two-step increase was attributed to the onset of TRS breaking associated with charge order, followed by an additional response, likely linked to a nematic state. In $Nb_{0.07}$-CVS, however, we observe a single TRS breaking transition. Regarding the enhanced TRS breaking signal near the surface in $Nb_{0.07}$-CVS, it mirrors what we previously noted in undoped RbV_3Sb_5[13], though in this case, the enhancement is two-fold rather than the five-fold increase seen in RbV_3Sb_5, which also displayed a more substantial rise in the onset temperature. In Ta-doped CsV_3Sb_5, where charge order is fully suppressed, no surface enhancement of TRS breaking was observed. In $Nb_{0.07}$-CVS, where charge order is partially suppressed, we observe a modest enhancement of TRS breaking near the surface. This suggests a correlation between the degree of surface enhancement and the strength of charge order. The observation that TRS breaking occurs at a lower temperature than the onset of bulk charge order in Nb-CVS is reminiscent of our previous finding in undoped compounds[5,10,31], where an additional increase in the zero-field relaxation rate was observed at temperatures below the charge-order onset. This also echoes recent theoretical work suggesting that TRS breaking—when driven by an electronic excitonic order—can coexist with charge order, even when the two phenomena emerge at distinct temperatures[38,39]. An ongoing theoretical question is how charge order, electronic order, and TRS breaking intertwine, and how this interplay may differ between the bulk and the surface.

(2) The superfluid density of $Nb_{0.07}$-CVS substantially increases with pressure. Within 1 GPa of applied pressure, T_C increased from 4.5 to 7 K, the superfluid density doubled, and the gap size tripled. For this to occur, we assume that the charge order is suppressed with pressure, as has been measured in other AV_3Sb_5 compounds[10,12]. The nearly linear scaling between the superconducting transition temperature (T_C) and superfluid density is a hallmark of unconventional superconductivity. Combined with our previous observations of undoped vanadium-based kagome superconductors under pressure[10,12], this scaling suggests a generic characteristic of kagome superconductors and provides compelling evidence of unconventional superconductivity in these materials. Additionally, the sharp and well-defined transition from the low-T_C to high-T_C state strongly indicates a first-order phase transition in $Nb_{0.07}$-CVS. It is worth noting that the maximum T_C that is achieved in kagome materials, such as Ta-doped CsV_3Sb_5[40], is only once charge order is suppressed (with maximal chemical doping $T_C \sim 5$ K). Hydrostatic pressure can also suppress charge order, but can elevate T_C to as high as 7–8 K in both undoped CsV_3Sb_5 and $Nb_{0.07}$-CVS. Unlike pressure, chemical doping typically introduces more disorder, which suggests that disorder negatively impacts T_C. Therefore, pressure

Table 1 | Summary of superconducting gap structure parameters at different hydrostatic pressures

Pressure (GPa)	0	0.4	0.8	1.2
$\lambda^{-2}(T=0)(\mu m^{-2})$	6.9(3)	5.7(3)	10.0(4)	12.5(1)
$\lambda(T>0)$ (nm)	381	419	315	283
ω	1	1	0.73(4)	1
T_C (K)	3.000(6)	3.25(1)	6.67(7)	6.94(2)
Δ_1 (meV)	0.54(9)	0.47(7)	0.65(5)	1.56(4)
Δ_2 (meV)	–	–	3.5(9)	–
χ^2	4.5	2.6	15.4	34.8
χ^2/NDF	0.346	0.153	1.1	1.74

0, 0.4 and 1.2 GPa data were fit with a single nodeless *s*-wave gap, whereas the 0.8 GPa data were fit with a double nodeless *s*-wave gap. λ is the London penetration depth, ω is the phase fraction, Δ is the size of the gap, and χ^2 and χ^2/NDF (number degrees of freedom) are goodness-of-fit parameters.

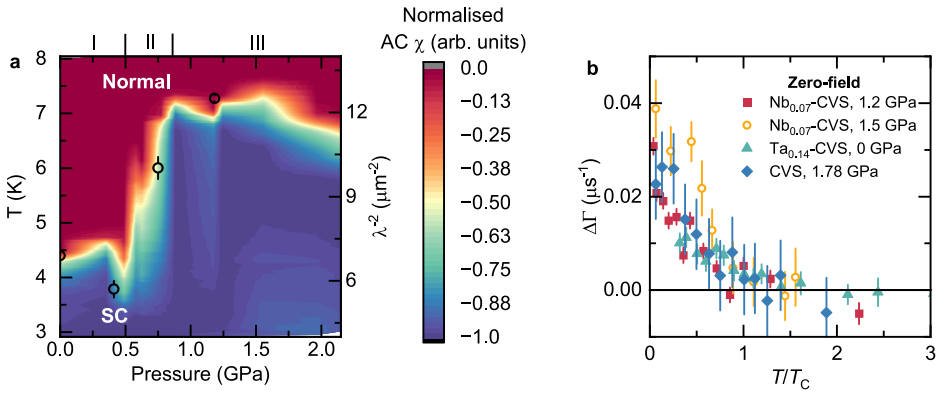

Fig. 6 | $Cs(V_{0.93}Nb_{0.07})_3Sb_5$ pressure phase diagram and comparison of time-reversal symmetry (TRS) breaking in CsV_3Sb_5 derived compounds. **a** AC susceptibility measurements as a function of applied hydrostatic pressure (0–2.2 GPa) have been normalised between −1 and 0 as described by the colour bar. The phase diagram is divided into three clear regions. Open circles show the inverse penetration depth squared, λ^{-2} (right axis), determined from the gap structure analysis of the muon-spin rotation data. **b** Comparison of TRS breaking across T_C for pure and doped CsV_3Sb_5 compounds. Single-crystal and polycrystalline samples are shown by closed and open markers, respectively. The *x*-axis has been scaled by a factor of T_C for each compound at that pressure. The error bars represent the standard deviation of the fit parameters.

emerges as a critical parameter for achieving the maximum possible T_C in these kagome materials, AV_3Sb_5.

(3) $Nb_{0.07}$-CVS exhibits a nodeless electron pairing, which is more pronounced under pressure as charge order is suppressed. Notably, ZF-μSR measurements below T_C at high pressure revealed an increase in relaxation rate, suggesting that TRS is broken in the superconducting state. As illustrated in Fig. 6b, this behaviour is not unique to $Nb_{0.07}$-CVS but aligns with findings across all CsV_3Sb_5-derived compounds examined by μSR[13,30]. Our results include compounds with suppressed charge order, such as $Ta_{0.14}$-CsV_3Sb_5 at ambient conditions[13] and undoped CsV_3Sb5 under 1.78 GPa pressure[12,30]. Furthermore, we demonstrate that this TRS-breaking behaviour is consistent across both single-crystal (closed red squares) and polycrystalline (open yellow circles) samples of $Nb_{0.07}$-CVS, indicating that the mechanism underpinning the TRS breaking is robust to disorder from doping and hydrostatic pressure. The combination of a fully gapped pairing state and time-reversal symmetry breaking is compatible with chiral $d_{x^2-y^2} + id_{xy}$ or triplet chiral $p_x + ip_y$ states (where i represents the imaginary unit)[41,42]. Together with the dilute superfluid density and its nearly linear scaling with the critical temperature, these findings underscore the unconventional pairing in this system. Finally, it is worth noting that superconducting transitions can, in principle, couple to the lattice through phonon modes interacting with the superconducting order parameter, potentially leading to lattice distortions. Such distortions may modify the local magnetic environment probed by muons and thus affect relaxation times. While these effects are likely small, the lack of a robust theoretical framework to quantify them or to distinguish them from those arising from TRS breaking makes it difficult to exclude their influence.

In conclusion, our work represents the most comprehensive microscopic study to date of both the normal and superconducting states in the doped kagome system $Nb_{0.07}$-CVS. We show that Nb doping decouples normal-state TRS breaking from charge order in the bulk, but synchronizes them near the surface. Additionally, we demonstrate how pressure drives the transition from a depth-tunable TRS-breaking normal state to a TRS-breaking superconducting state with significantly enhanced superfluid density and an increased superconducting critical temperature. This sheds light on the complex interplay between charge order, TRS breaking, and unconventional superconductivity in kagome materials. These findings highlight the pressing need for a comprehensive theoretical framework to uncover the fundamental mechanisms behind TRS breaking in superconductors, particularly given the unresolved nature of the order parameters in canonical TRS-breaking superconductors like UTe_2[43,44] and Sr_2RuO_4[45,46].

Methods

Muon spin rotation/relaxation (μSR)

In a muon spin rotation/relaxation (μSR) experiment, a beam of nearly 100% spin-polarised muons, μ^+ is implanted into the sample, one muon at a time. These positively charged μ^+ particles stop, due to thermal stabilisation, at interstitial lattice sites in the crystal. The muon will then precess at a frequency proportional to the local internal magnetic field, B_μ, before decaying into a positron, which is preferentially emitted in the direction of the muon spin, which is then detected.

Experimental details

Zero-field (ZF), weak transverse-field (TF) and longitudinal-field (LF) μSR measurements, exploring both the superconducting and normal states, were performed on the GPS and Dolly instruments[47] at the Swiss Muon Source (SμS), Paul Scherrer Institute, Villigen, Switzerland. On GPS, a continuous flow cryostat was used to measure temperatures in the range of 1.5–300 K. Large single crystals were placed in a mosaic arrangement, and the muon spin was rotated so that the measurements were sensitive to both the *ab* plane and *c*-axis. A weak transverse field of 10 mT was applied for measurements in the normal state. For LF measurements, a field of 2.5–20mT was applied, which was sufficient to fully decouple the muon spin from the internal magnetic field. Additional measurements were conducted on the high-field instrument, HAL, also at SμS. Here, the applied field ranged from 10 mT to 8 T. Data in Fig. 2c were fit with the following equation:

$$A_{\mathrm{TF}}(t) = A_i \exp(-\sigma_i t) \cos\left(\gamma_\mu B_{\mathrm{int},i} t + \varphi\right) \tag{3}$$

where A_i is the asymmetry, σ_i is the relaxation rate, γ_μ is the gyromagnetic ratio of the muon, $B_{\mathrm{int},i}$ is the internal magnetic field, and φ is the phase shift.

ZF and weak TF μSR experiments were conducted on single-crystal samples of $Nb_{0.07}$-CVS using the low-energy μSR instrument LEM at the Swiss Muon Source (SμS), Paul Scherrer Institute, Villigen, Switzerland[34,48]. Large single-crystals, covering a total area of 2×2 cm^2 were arranged in a mosaic layout on a nickel-coated plate and adhered with silver paste. The sample was mounted on a cold finger cryostat, allowing temperatures of 5–300 K to be accessed. The muon beam can be adjusted to energies between 1 and 30 keV. The implantation energy, E corresponds to a specific muon implantation depth profile, allowing us to measure implantation depths between a few nanometres up to several tens of nanometres. In this experiment, the depths we probed were between $\bar{z} = 1 - 120$ nm. In both, Fig. 3a and d, we have provided a conversion between E and $\bar{z}$. The muon implantation profiles in $Nb_{0.07}$-CVS for different implantation energies were simulated using the TrimSP Monte Carlo algorithm[34].

ZF and TF μSR experiments under pressure were performed at the high-pressure spectrometer GPD[49] at the Swiss Muon Source (SμS), Paul Scherrer Institute, Villigen, Switzerland. Randomly oriented single-crystal samples of $Nb_{0.07}$-CVS were loaded into a pressure cell in a compact cylindrical area of height 12 mm and diameter of 6 mm. The double-wall pressure cell was made of an MP35N/CuBe alloy, specifically designed for high-pressure experiments and can reach applied pressures of 2.8 GPa at room temperature. Daphne 7373 oil was used as a pressure medium to reach the highest pressures. The

pressure was determined by tracking the superconducting transition of indium using AC magnetic susceptibility measurements. These AC measurements were also used to construct the pressure phase diagram using an in-house Janis cryostat, which is controlled through the flow of liquid helium. Indium transitions were removed from the data for clarity.

Superconducting gap structure

To perform a quantitative analysis of μSR data and determine the superconducting gap structure, the superconducting muon spin depolarisation rate, $\sigma_{sc}(T)$, in the presence of a perfect triangular vortex lattice is first related to the London penetration depth, $\lambda(T)$ by the following equation[50,51]:

$$\frac{\sigma_{sc}(T)}{\gamma_{\mu}} = 0.06091\frac{\Phi_0}{\lambda^2(T)} \tag{4}$$

where $\Phi_0 = 2.068 \times 10^{15}$ Wb is the magnetic flux quantum. This equation is only applicable when the separation between vortices is larger than λ. In this particular case, as per the London model, σ_{sc} becomes field-independent. By analysing the temperature of the magnetic penetration depth, within the local London approximation, a direct association with the superconducting gap symmetry can be made[29]:

$$\frac{\lambda^{-2}(T,\Delta_{0,i})}{\lambda^{-2}(0,\Delta_{0,i})} = 1 + \frac{1}{\pi}\int_0^{2\pi}\int_{\Delta(T,\phi)}^{\infty}\left(\frac{\delta f}{\delta E}\right)\frac{E\mathrm{d}E\mathrm{d}\varphi}{\sqrt{E^2-\Delta_i(T,\varphi)^2}} \tag{5}$$

where $f = \left[1+\exp(E/k_BT)\right]^{-1}$ is the Fermi function, φ is the angle along the Fermi surface, and $\Delta_i(T,\varphi) = \Delta_{0,i}\Gamma(T/T_C)g(\varphi)$ ($\Delta_{0,i}$ is the maximum gap value at $T = 0$). The temperature dependence of the gap is approximated by the expression, $\Gamma\left(T/T_C = \tanh 1.82\left[1.018(T_C/T-1)\right]^{0.51}\right.$[52], whilst $g(\varphi)$ describes the angular dependence of the new gap and is replaced by 1 for an s-wave gap, $[1 + a\cos(4\varphi)/(1 + a)]$ for an anisotropic s-wave gap, and $|\cos(2\varphi)|$ for a d-wave gap[53].

Data availability

All related data are available from the authors. Alternatively, all the muon-spin rotation data can be accessed through the SciCat data base using the following links: GPS: https://doi.org/10.16907/83b854b1-00fd-43e2-9d25-fa5d2d2eac07 LEM: https://doi.org/10.16907/1c2661e3-769b-4cdf-8504-4959fff59d17, and other data at http://musruser.psi.ch/cgi-bin/SearchDB.cgi using the following details: 1. Area: Dolly, Year: 2023, Run Title: CVS-Rb..., Run: 0263-0291 (named incorrectly in file). 2. Area: HAL, Year: 2023, Run Title: CVS..., Run: 0047-0182. 3. Area: GPD, Year: 2024, Run Title: Nb-CVS..., Run: 0067-0181.

Received: 5 February 2025; Accepted: 16 July 2025;
Published online: 02 August 2025

References

1. Giustino, F. et al. The 2021 quantum materials roadmap. *J. Phys.: Mater.* **3**, 042006 (2021).
2. Neupert, T., Denner, M. M., Yin, J.-X., Thomale, R. & Hasan, M. Z. Charge order and superconductivity in kagome materials. *Nat. Phys.* **18**, 137–143 (2022).
3. Khatua, J. et al. Experimental signatures of quantum and topological states in frustrated magnetism. *Phys. Rep.* **1041**, 1–60 (2023).
4. Yin, J.-X., Lian, B. & Hasan, M. Z. Topological kagome magnets and superconductors. *Nature* **612**, 647–657 (2022).
5. Guguchia, Z., Khasanov, R. & Luetkens, H. Unconventional charge order and superconductivity in kagome-lattice systems as seen by muon-spin rotation. *npj Quantum Mater.* **8**, 41 (2023).
6. Wang, Y., Wu, H., McCandless, G. T., Chan, J. Y. & Ali, M. N. Quantum states and intertwining phases in kagome materials. *Nat. Rev. Phys.* **5**, 635–658 (2023).
7. Wilson, S. D. & Ortiz, B. R. AV_3Sb_5 kagome superconductors. *Nat. Rev. Mater.* **9**, 420–432 (2024).
8. Deng, H. et al. Chiral kagome superconductivity modulations with residual Fermi arcs. *Nature* **632**, 775–781 (2024).
9. Ortiz, B. R. et al. New kagome prototype materials: discovery of KV_3Sb_5, RbV_3Sb_5, and CsV_3Sb_5. *Phys. Rev. Mater.* **3**, 094407 (2019).
10. Guguchia, Z. et al. Tunable unconventional kagome superconductivity in charge ordered RbV_3Sb_5 and KV_3Sb_5. *Nat. Commun.* **14**, 153 (2023).
11. Jiang, K. et al. Kagome superconductors AV_3Sb_5 (A = K, Rb, Cs). *Natl Sci. Rev.* **10**, nwac199 (2023).
12. Gupta, R. et al. Microscopic evidence for anisotropic multigap superconductivity in the CsV_3Sb_5 kagome superconductor. *npj Quantum Mater.* **7**, 49 (2022).
13. Graham, J. N. et al. Depth-dependent study of time-reversal symmetry-breaking in the kagome superconductor AV_3Sb_5. *Nat. Commun.* **15**, 8978 (2024).
14. Liu, Y. et al. Enhancement of superconductivity and suppression of charge-density wave in As-doped CsV_3Sb_5. *Phys. Rev. Mater.* **6**, 124803 (2022).
15. Li, J. et al. Strong-coupling superconductivity and weak vortex pinning in Ta-doped CsV_3Sb_5 single crystals. *Phys. Rev. B* **106**, 214529 (2022).
16. Liu, M. et al. Evolution of superconductivity and charge density wave through Ta and Mo doping in CsV_3Sb_5. *Phys. Rev. B* **106**, L140501 (2022).
17. Liu, Y. et al. Doping evolution of superconductivity, charge order, and band topology in hole-doped topological kagome superconductors $Cs(V_{1-x}Ti_x)_3Sb_5$. *Phys. Rev. Mater.* **7**, 064801 (2023).
18. Hou, J. et al. Effect of hydrostatic pressure on the unconventional charge density wave and superconducting properties in two distinct phases of doped kagome superconductors $CsV_{3-x}Ti_xSb_5$. *Phys. Rev. B* **107**, 144502 (2023).
19. Zhong, Y. et al. Nodeless electron pairing in CsV_3Sb_5-derived kagome superconductors. *Nature* **617**, 488–492 (2023).
20. Liu, J. et al. Enhancement of superconductivity and phase diagram of Ta-doped kagome superconductor CsV_3Sb_5. *Sci. Rep.* **14**, 9580 (2024).
21. Mydosh, J. A. Spin glasses: redux: an updated experimental/materials survey. *Rep. Prog. Phys.* **78**, 052501 (2015).
22. Clark, L. & Abdeldaim, A. H. Quantum spin liquids from a materials perspective. *Annu. Rev. Mater. Res.* **51**, 495–519 (2021).
23. Shi, C. et al. Annealing-induced long-range charge density wave order in magnetic kagome FeGe: Fluctuations and disordered structure. *Sci. China Phys. Mech. Astron.* **67**, 117012 (2024).
24. Ortiz, B. R. et al. CsV_3Sb_5: a Z2 topological kagome metal with a superconducting ground state. *Phys. Rev. Lett.* **125**, 247002 (2020).
25. Zhu, C. et al. Double-dome superconductivity under pressure in the v-based kagome metals AV_3Sb_5 (A = Rb and K). *Phys. Rev. B* **105**, 094507 (2022).
26. Nakayama, K. et al. Multiple energy scales and anisotropic energy gap in the charge-density-wave phase of the kagome superconductor CsV_3Sb_5. *Phys. Rev. B* **104**, L161112 (2021).
27. Yan, X.-Y. et al. Chiral pair density waves with residual Fermi arcs in RbV_3Sb_5. *Chin. Phys. Lett.* **41**, 097401 (2024).
28. Zhao, C. et al. Ultralow-temperature heat transport evidence for residual density of states in the superconducting state of CsV_3Sb_5. *Chin. Phys. Lett.* **41**, 127303 (2024).
29. Suter, A. & Wojek, B. Musrfit: a free platform-independent framework for μSR data analysis. *Phys. Procedia* **30**, 69–73 (2012). *International Conference on Muon Spin Rotation, Relaxation and Resonance (μSR2011)*.
30. Khasanov, R. et al. Time-reversal symmetry broken by charge order in CsV_3Sb_5. *Phys. Rev. Res.* **4**, 023244 (2022).

31. Bonfà, P. et al. Unveiling the nature of electronic transitions in RbV_3Sb_5 with avoided level crossing μsr. arXiv preprint arXiv:2411.04848 (2024).
32. Mielke III, C. et al. Nodeless kagome superconductivity in $LaRu_3Si_2$. *Phys. Rev. Mater.* **5**, 034803 (2021).
33. Mielke III, C. et al. Time-reversal symmetry-breaking charge order in a kagome superconductor. *Nature* **602**, 245–250 (2022).
34. Morenzoni, E. et al. Implantation studies of keV positive muons in thin metallic layers. *Nucl. Instrum. Methods Phys. Res. Sect. B: Beam Interact. Mater. At.* **192**, 254–266 (2002).
35. Das, D. et al. Time-reversal invariant and fully gapped unconventional superconducting state in the bulk of the topological compound $Nb_{0.25}Bi_2Se_3$. *Phys. Rev. B* **102**, 134514 (2020).
36. Chen, X. et al. Highly robust reentrant superconductivity in CsV_3Sb_5 under pressure. *Chin. Phys. Lett.* **38**, 057402 (2021).
37. Luke, G. M. et al. Time-reversal symmetry-breaking superconductivity in Sr_2RuO_4. *Nature* **394**, 558–561 (1998).
38. Ingham, J., Thomale, R. & Scammell, H. D. Vestigial order from an excitonic mother state in kagome superconductors AV_3Sb_5. arXiv preprint arXiv:2503.02929 (2025).
39. Scammell, H. D., Ingham, J., Li, T. & Sushkov, O. P. Chiral excitonic order from twofold van Hove singularities in kagome metals. *Nat. Commun.* **14**, 605 (2023).
40. Deng, H. et al. Evidence for time-reversal symmetry-breaking kagome superconductivity. *Nat. Mater.* **23**, 1639–1644 (2024).
41. Wu, X. et al. Nature of unconventional pairing in the kagome superconductors AV_3Sb_5 (A = K, Rb, Cs). *Phys. Rev. Lett.* **127**, 177001 (2021).
42. Kiesel, M. L. & Thomale, R. Sublattice interference in the kagome Hubbard model. *Phys. Rev. B* **86**, 121105 (2012).
43. Ran, S. et al. Nearly ferromagnetic spin-triplet superconductivity. *Science* **365**, 684–687 (2019).
44. Aoki, D. et al. Unconventional superconductivity in heavy fermion UTe_2. *J. Phys. Soc. Jpn.* **88**, 043702 (2019).
45. Grinenko, V. et al. Split superconducting and time-reversal symmetry-breaking transitions in Sr_2RuO_4 under stress. *Nat. Phys.* **17**, 748–754 (2021).
46. Maeno, Y., Yonezawa, S. & Ramires, A. Still mystery after all these years-unconventional superconductivity of Sr_2RuO_4. *J. Phys. Soc. Jpn.* **93**, 062001 (2024).
47. Amato, A. et al. The new versatile general purpose surface-muon instrument (GPS) based on silicon photomultipliers for μsr measurements on a continuous-wave beam. *Rev. Sci. Instrum.* **88**, 093301 (2017).
48. Prokscha, T. et al. The new μE4 beam at PSI: a hybrid-type large acceptance channel for the generation of a high intensity surface-muon beam. *Nucl. Instrum. Methods Phys. Res. Sect. A* **595**, 317–331 (2008).
49. Khasanov, R. Perspective on muon-spin rotation/relaxation under hydrostatic pressure. *J. Appl. Phys.* **132**, 190903 (2022).
50. Brandt, E. H. Flux distribution and penetration depth measured by muon spin rotation in high-T_c superconductors. *Phys. Rev. B* **37**, 2349–2352 (1988).
51. Brandt, E. H. Properties of the ideal Ginzburg–Landau vortex lattice. *Phys. Rev. B* **68**, 054506 (2003).
52. Carrington, A. & Manzano, F. Magnetic penetration depth of MgB_2. *Physica C* **385**, 205–214 (2003).
53. Fang, M. H. et al. Superconductivity close to magnetic instability in $Fe(Se_{1-x}Te_x)_{0.82}$. *Phys. Rev. B* **78**, 224503 (2008).

Acknowledgements

The μSR experiments were carried out at the Swiss Muon Source (SμS), Paul Scherrer Institute, Villigen, Switzerland. Z.G. acknowledges support from the Swiss National Science Foundation (SNSF) through SNSF Starting Grant (No. TMSGI2_211750). Z.G. acknowledges the useful discussions with Robert Scheuermann. The work at BIT was supported by the National Key R&D Program of China (Nos. 2020YFA0308800 and 2022YFA1403400), the National Natural Science Foundation of China (No. 92065109), the Beijing National Laboratory for Condensed Matter Physics (Grant No. 2023BNLCMPKF007), and the Beijing Natural Science Foundation (Grant No. Z210006). Z.W. thanks the Analysis & Testing Center at BIT for assistance with facility support.

Author contributions

Z.G. conceived, designed, and supervised the project. Crystal growth: Y.L., Y.Y. and Z.W. μSR and AC susceptibility experiments under ambient pressure as well as the corresponding discussions: J.N.G., S.S.I., V.S., G.J., P.K., O.G., A.D., I.B., J.C., Z.S., A.S., T.P., H.L., R.K. and Z.G. μSR and AC susceptibility experiments under pressure: J.N.G., S.S.I. and Z.G. μSR data analysis: J.N.G. and Z.G.. STM experiments and corresponding discussions: H.D., J.N.G., Z.G. and J.-X.Y. ARPES experiments and corresponding discussions: Y.Z., Z.G. and K.O. Figure development and writing of the paper: J.N.G. and Z.G., with contributions from all authors. All authors discussed the results, interpretation, and conclusion.

Competing interests

The authors declare no competing interests.

Additional information

Supplementary information The online version contains supplementary material available at https://doi.org/10.1038/s42005-025-02235-6.

Correspondence and requests for materials should be addressed to Zhiwei Wang or Zurab Guguchia.

Peer review information *Communications Physics* thanks the anonymous reviewers for their contribution to the peer review of this work.